

Experimental analysis of basal wall friction coefficient for a velocity controlled confined granular flow

Li Yu Lai¹, Fu-Ling Yang^{1,*}

¹ National Taiwan University, Department of Mechanical Engineering, No. 1, Sec. 4, Roosevelt Rd., Taipei 10617, Taiwan.

Abstract. This work presents a novel experimental design to measure the effective wall friction coefficient μ_w between a confined granular material and a flat wall under a controlled relative velocity and normal load, with concurrent monitoring of the solid volume fraction of the interacting layer. The design allows us to investigate the effects of initial packing configuration, in random or face-centered-cubic packing. The μ_w is further scaled by the particle-wall pure sliding friction coefficient, μ_{pw} , with the normal load considered to infer the degree of incoherent particle dynamics when discrete particles may develop rolling but not pure sliding contacts. Reverse μ_w/μ_{pw} variation trends with the sliding velocity are found and explained.

1 Introduction

Granular flow occurs widely in both natural and industrial contexts, necessitating accurate modeling and prediction. Both the constitutive relations and effective boundary condition models are essential, but the latter is treated very differently in the literature and requires further investigation. Some adopt the velocity boundary condition: the slip condition for dilute and moderately dense flows [1, 2], and the no-slip condition in dense flows [3, 4]. A stress boundary condition is equally popular when the bulk moves relative to a solid boundary and a Coulomb-type wall shear stress, $\tau_w = \mu_w p$, is assigned depending on the wall normal pressure p and a wall friction coefficient μ_w . Early works assume a constant μ_w [5, 6], but recent simulations of confined granular flows report a non-constant side-wall μ_w that decreases with depth in both steady inclined surface flows [7] and transient avalanche processes [8]. If we examine μ_w with the relative sliding velocity between the bulk and the solid boundary, μ_w is found to decay with the sliding velocity, which agrees with the experimental findings for steady inclined surface flows [11].

Non-constant μ_w was detected at the side wall of a top-loaded granular annular shear cell [9]. Interestingly, μ_w also decays with the sliding velocity when the top load is large, but a reverse trend in which μ_w grows with diminishing velocity can be observed when the minimum top load is used. However, such a reverse trend of μ_w rising with dropping velocity was also detected in a tribology test of confined granular material subject to very heavy loads [10]. Clearly, the normal load affects how μ_w varies with the sliding velocity for a confined granular flow, but the literature data show inconsistent trends, necessitating further research. In fact, non-constant μ_w has been explained by the degree of incoherent particle translation [7, 9,10] or rotation [8,9] relative to the sliding velocity, which shall result from unbalanced particle interactions with each other and with the solid boundary. These particle-level dynamics shall vary with the packing configuration, the solid volume fraction ϕ of the layer adjacent to the solid boundary, and

the normal load, which properties are often unaddressed. Hence, this work designs an experiment where the top load and the base sliding velocity can be imposed onto a confined granular packing to measure its μ_w and ϕ of the contacting layer. Grain-level dynamics are not measured, but we aim to provide evidence for how changes in the normal load and the packing configuration can reverse the μ_w variation trend with the sliding velocity, in view of the corresponding changes in ϕ .

2 Experiment Setup

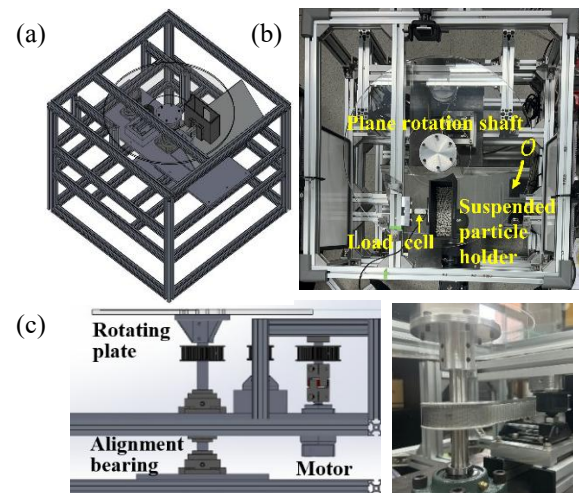


Fig.1 (a) Schematic diagram of the test facility, (b) top view of the test facility with the key components annotated, (c) the layout of the driving mechanism (side view) and the connecting toothed belt.

Figure 1(a) presents the schematic diagram of the test facility in a layered structure built to an aluminum box frame. The top view of the actual facility is given in **Fig.1(b)**. The lower two layers are heavy metal plates that hold a vertical steel shaft through a pair of alignment bearings, as shown in **Fig.1(c)**. A transparent acrylic plate of 1cm thickness and $R=25\text{cm}$ radius is fixed horizontally on the shaft at the mid-height of the frame, which is driven by a toothed belt fit to the gear fixed on the vertical shaft, as shown on the right subplot of **Fig.1(c)**. The belt was driven by another gear fixed to the shaft of an upright

* Corresponding author: fulingyang@ntu.edu.tw

AC motor (Panasonic, Servomotor 3000 RPM 200V) installed sideways. Via this setting, the plate can be rotated steadily at an angular speed of $\Omega=20, 30, 45, 60,$ and 75 rpm, confirmed by a portable tachometer.

On top of the base rotating plate, a suspended holder of internal size 13cm in length, 5cm in width, and 12cm in height was designed and 3D-printed to confine the test particles as shown by the black box in **Fig.1(b)** and **Fig.2(a)**. Special care was made to suspend the holder at a $d/2$ vertical clearance above the rotating plate, to avoid physical contact between the holder and the plate. The width was chosen to prevent a secondary circulating flow via visual inspection of the grain dynamics. A lateral slot was designed and 3D-printed on one sidewall (the leading side, in view of the base plate motion) to hold a fixture screwed to the load cell (Transcell, ST4) as shown in **Fig.2(b)**. The load cell was then fixed to a top horizontal aluminum extrusion bar to complete the suspended holder and load-cell module. The holder was carefully positioned so that the sidewall attached to the load cell is perpendicular to the circumference of the rotating plate, with the load cell set precisely at $R/2$ from the center of the rotation base.

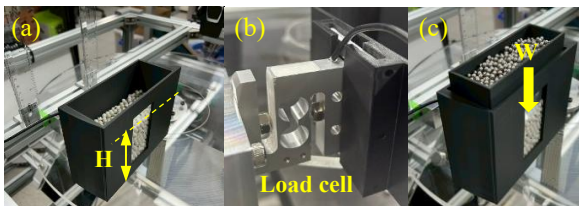


Fig.2 (a) The suspended holder and confined particles atop the plate, (b) the load-cell locked with the holder, (c) top weight W added by another box of steel beads.

In the holder, we filled the test particles to a specific height H , as marked on **Fig.2(a)**. A top box that can fit into the holder was 3D-printed, with its outer dimension shrinking 1mm from the holder's interior, as shown in **Fig.2(c)**. We added steel beads in the top box to apply different normal weights $W=450$ and 1050 gw on the test spheres, made of Polyoxymethylene (POM) with a mean diameter of $d=0.59\pm 0.001$ cm, and an intrinsic density of $\rho_s=1.91\pm 0.01$ g/cm³. To monitor the particle configuration in the basal layer, a 45°-tilt mirror was installed beneath the transparent rotating plate to reflect the basal image towards a lateral high-speed digital camera, as shown in **Fig.3**.

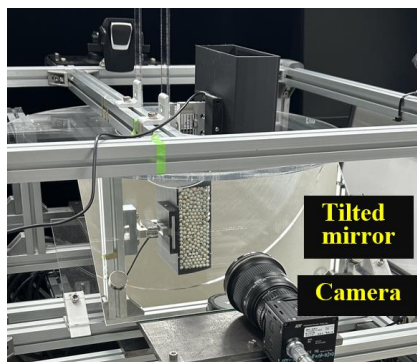


Fig.3 Bottom view of the basal particles reflected by a 45°-tilt mirror to a lateral high-speed digital camera.

3 Force and Image Signal Processing

3.1 Force data and its filter

Once the base plate motion is activated, the particles are forced to move relative to the plate, resulting in a pulling force $F(t)$ on the holder, recorded by the load cell at a 2kHz via a data acquisition system (NI cDAQ-9178, NI9949, and NI9237). The voltage signal is converted to force with a self-calibrated linear relation. **Fig.4** presents the instantaneous force signals $F(t)$ for the static condition (marked by System Noise), and for the signals when no and different amounts of particles (denoted by the initial packing height H) were driven at $\Omega=20$ rpm. The temporal mean friction grows with H to indicate a greater hindrance when a thicker layer is dragged, which implies promoted inter-particle friction and interlocking between different particle layers.

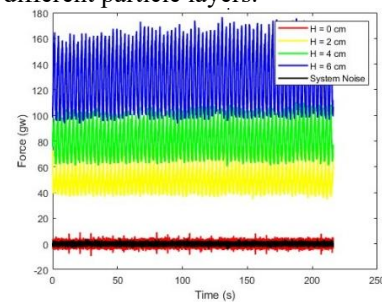


Fig.4 Instantaneous force signal in different operations.

Comparing the data when the base plate was operated with no filled particles ($H=0$ cm, in red) to the system noise (in black), the amplified temporal fluctuation suggests mechanical resonance of the suspended holder. The fluctuation magnitude also grows with H , suggesting a raised resonating mass. These temporal fluctuations draw our attention to filter out unwanted force signals from structural vibrations. Hence, the force spectra for the data presented in **Fig.4** are examined in **Fig.5** over different frequency bands to identify the troublesome frequencies. The reference spectrum when the plate is operated without any particles, $F_0(\omega)$, is shown in green to assist comparison, where the subscript in the rest subplots marks the initial packing height $H=0$.

In the lowest frequency range of 0-10 Hz in **Fig.5(a)**, the force signal peaks at multiples of the base rotation frequency $\Omega/60$ Hz when particles were filled, indicating particle-plate interaction. The peaks at higher frequencies with $H=2$ cm are suppressed when H is raised, suggesting a loss of total kinetic energy that scales with the sum of the squares of the frequency spectrum. This phenomenon agrees with the finding of a greater mean hindrance observed in **Fig.4**. The other groups of persistent force peaks are found at the harmonics of 60Hz in the high frequency band of 120-1000 Hz (not shown). These peaks result from the electromagnetic interference of the AC motor operated with the 60 Hz AC current, and hence shall also be removed.

In between over 40-120 Hz, intriguing spectra are observed where a few peaks were observed to persist through the tests with or without the particles, as marked by the gray arrows on the reference spectrum in **Fig.5(c)**, and shall represent the structural vibration modes. We first identify at what frequency the $F_0(\omega_i)$ (no particles)

exceeds the corresponding temporal mean (in **Fig.4**) plus one temporal standard deviation. These reference peaks are used to scrutinize the force spectra, $F_H(\omega_i)$, when particles are filled to different heights (denoted in the subscript) over the range of $\omega_i \pm 4\text{Hz}$. Only when the difference between all the spectra is lower than the nominal noise level of $\pm 20\text{dB}$, with $F_0(\omega_i)/\sqrt{2} \leq F_H(\omega_i \pm 4\text{Hz}) \leq \sqrt{2}F_0(\omega_i)$, the ω_i is identified as the system vibration modes. The harmonics of $\Omega/60\text{Hz}$, 60Hz , and the identified ω_i are adopted to define a set of zero-window functions with a $\pm 4\text{ Hz}$ span to form the force filter for this test facility.

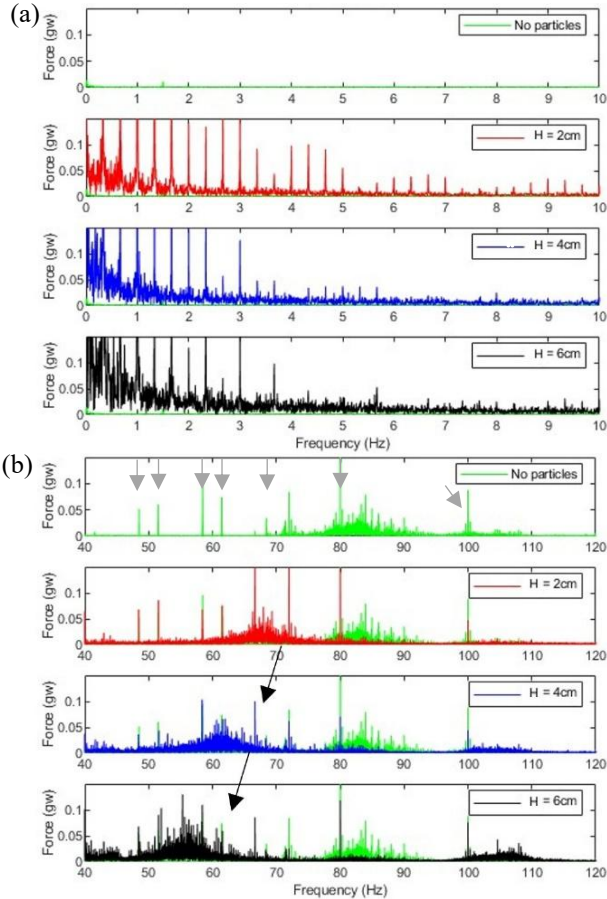


Fig.5 Force spectrum in (a) low and (b) medium frequency bands when randomly poured particles of different amounts (indicated by H) are driven by the base plate rotation at $\Omega=20\text{ rpm}$ without extra loading ($W=0$).

One final remark is given to **Fig.5(c)** where $F_H(\omega)$ shows a fat triangular spectrum that appeared only when particles were filled, and hence must result solely from the particle-plate interactions. The wide spectrum shows no intrinsic time scale in the process. The shift of the spectrum towards the lower frequency with rising H (marked by the long black arrows) shall correspond to the rising resonating mass of the suspended holder marked before from the temporal fluctuation amplitudes in **Fig.4**, like how the simple harmonic resonance frequency of a mass-spring system diminishes with the mass.

3.2 Image analysis for solid volume fraction

To estimate ϕ for the basal layer, we first converted an instantaneous particle image into a light intensity field $I(t, x, y)$ and applied the circular Hough method to locate

individual particles as marked in the left inset of **Fig.6(a)**. Artificial disks were created from these centers with the known radius (in pixels) to generate a binary image as the right inset of **Fig.6(a)**. An observation window was defined at the center of the holder to avoid boundary effects on the packing configuration. The total number of white particle pixels in the observation window is divided by the window size to find an instantaneous projection area ratio, $A_p(t)$, which estimates the volume fraction of the basal layer by $\phi(t)=2/3A_p(t)$, with 2/3 being the volume ratio of a sphere to the cylinder circumscribing it. Such an evaluation underestimates the actual $\phi(t)$ as top particles can fill in the gaps between the spherical particles, but it can qualitatively distinguish the packing compactness in different tests. For each test, 100 instantaneous $\phi(t)$ were calculated to evaluate a mean ϕ .

4 Tests and results

To test the effect of packing ϕ , an initial packing in the face-centered cubic configuration (denoted by FCC) was prepared, in addition to the randomly-poured packings (denoted by RAN). For both filling methods, the particles were packed to the same initial height of $H=8\text{cm}$ for the friction force measurement, which weighed 577.67gw (RAN) and 579.37gw (FCC). The added top weights W could generate a total normal load roughly 1.77 and 2.8 times larger than the particle weights. The force signal exhibits the aforementioned spectrum features and was filtered as described, and converted to the time domain. The temporal mean of the filtered signal gives the steady friction force F_T , resulting solely from the particle-plate interactions, and a division by the total normal load, particles' weight plus W , determines the basal effective friction coefficient, μ_w . Independent sliding table tests were conducted to evaluate the particle-plate pure sliding friction coefficient subjected to these specific total normal loads in the increasing order, giving $\mu_{pw}=0.4394$, 0.3516 , and 0.3105 . These values are used to scale the effective basal friction coefficient as μ_w/μ_{pw} , and a value below unity suggests that there are particles undergoing rolling but not pure sliding contacts during the observation duration. The former is known to render a particle-wall friction coefficient lower than μ_{pw} [7].

Fig.6(a) and **6(b)** present the mean ϕ and the μ_w/μ_{pw} with increasing O (equivalent to the relative sliding velocity examined in the literature). The data from an initially FCC or random packing are distinguished by their subscripts, FCC or RAN. Apparently, the packing style critically affects the magnitude of ϕ and its variation trend with O and W . A static FCC packing possesses a greater ϕ_{FCC} than ϕ_{RAN} , and particles therein experience frictional contacts at a greater frequency and in a more coherent pattern to form a more stable force network, better withstanding shear-induced perturbations. Without extra normal load, ϕ_{FCC} in general dilates slightly with O , while the corresponding $\mu_w/\mu_{pw}|_{\text{FCC}} \approx 0.62$ remains nearly unchanged in **Fig.6(b)** (blue dashed lines). Adding W deformed the initial packing structure to engage more and stronger frictional contacts into a more stable network than that with $W=0$. The heavy load may also push the static basal particles further apart which shall

further dilatate upon basal shearing to induce a slightly lower $\phi|_{FCC,W}$ (red and orange dashed lines in **Fig.6(a)**). To ensure total mass conservation, compaction shall take place in the top layers, which further strengthens the contact network therein. Such a stronger network imposed a greater impulse from atop to prevent the particles in the basal layer from free rotations. Hence, rolling contacts are less likely to occur than pure sliding contact, so that the $\mu_w/\mu_{pw}|_{FCC,W} > 0.65$ in **Fig.6(b)** always exceeding the nearly constant value $\mu_w/\mu_{pw}|_{FCC} \approx 0.62$ without W. The same reason also explains why $\mu_w/\mu_{pw}|_{FCC,W}$ grows with W (the red dashed line falls below the orange dashed lines). Raising O promotes the perturbations to induce slight dilation in $\phi|_{FCC,W}$ and further compaction in the top layer. The O-and-W induced stronger top network suppresses the rolling contacts so that $\mu_w/\mu_{pw}|_{FCC,W}$ further grows above 0.7 with a growing O, signaling shear-thickening.

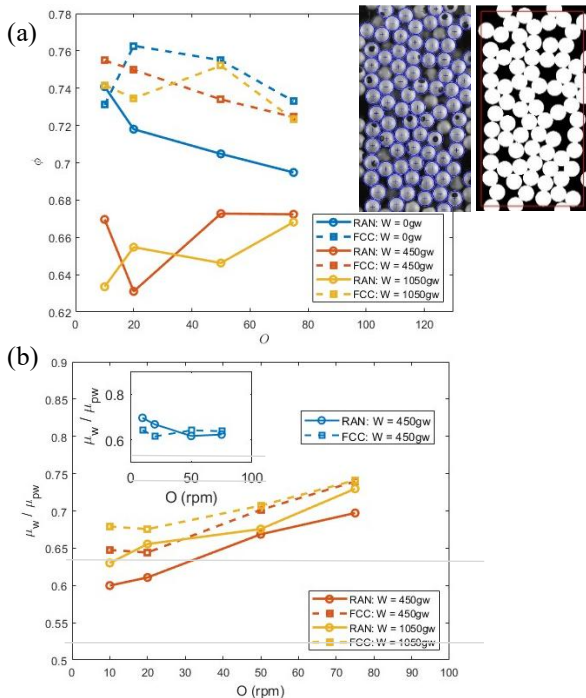


Fig.6 Variation of the (a) ϕ for the basal layer and (b) scaled μ_w/μ_{pw} with respect to O and W. The insets show a raw basal image with the particles located, and the converted binary image used to evaluate $\phi(t)$.

In contrast, particles in the looser random packing develop more incoherent frictional contacts and hence can rearrange more easily upon perturbations. Raising O without extra loading fluidizes the basal layer more easily so that $\phi|_{RAN}$ drops more severely with O than $\phi|_{FCC}$ (solid blue line). Particles in the looser basal layer can move more freely to develop more rolling contacts than pure sliding contacts, so that $\mu_w/\mu_{pw}|_{RAN}$ is found to decay with O to reveal a peculiar shear-thinning phenomenon. Adding sufficient top weights reversed the $\phi|_{RAN,W}$ -O correlation. The extra weight deformed the initial random packing to induce a network weaker than that formed from an FCC packing due to the incoherent configuration of frictional contacts. Hence, particles in the upper layer can still rearrange upon basal shearing and interlock to develop a denser top layer that pushes the randomly located particles in the basal layer further apart to induce

a much lower $\phi|_{RAN,W}$ than the rest cases. As the top-layer network is weaker than those from an FCC packing, raising O suffices to perturb the network and loosen particles therein, which rejoin the basal layer to cause slight compaction and hence the $\phi|_{RAN,W}$ -O rising trend. The slight freedom in the motions of the basal particles renders a consistently lower $\mu_w/\mu_{pw}|_{RAN,W} < 0.65$, than the value $\mu_w/\mu_{pw}|_{FCC,W}$. Similar behaviors are found for how $\mu_w/\mu_{pw}|_{RAN,W}$ grows with W and thickens with O, and shall be explained by the same mechanisms.

Undoubtedly, the rich results revealed in this work and the speculated particle bed responses require further rigorous research in view of particle dynamics analysis, both across the packing height and through the transient process. It is also worth integrating the current findings into the model proposed in the literature [8], if particle translation and rotation can be concurrently measured.

We acknowledge the financial support from the National Science and Technology Council, Taiwan, via the grants: 112-2221-E-002 -137 -MY3 and 113-2923-E-002-009.

Reference

1. J.T. Jenkins, M.W. Richman, Boundary conditions for plane flows of smooth, nearly elastic, circular disks. *J. Fluid Mech.* **171**, 53–69 (1986)
2. P. Mills, D. Loggia, M. Tixier, Model for a stationary dense granular flow along an inclined wall. *Europhys. Lett.* **45**, 733–738 (1999)
3. P. Mills, M. Tixier, D. Loggia, Influence of roughness and dilatancy for dense granular flow along an inclined wall. *Eur. Phys. J. E* **1**, 5–8 (2000).
4. S. Courrech du Pont, P. Gondret, B. Perrin, M. Rabaud, Wall effects on granular heap stability. *Europhys. Lett.* **61**, 492–498 (2003)
5. N. Taberlet, P. Richard, A. Valance, W. Losert, J.M. Pasini, J.T. Jenkins, R. Delannay, Superstable granular heap in a thin channel. *Phys. Rev. Lett.* **91**, 264301 (2003)
6. P. Richard, A. Valance, J.-F. Métayer, P. Sanchez, J. Crassous, M. Louge, and R. Delannay, Rheology of confined granular flows: scale invariance, glass transition, and friction weakening. *Phys. Rev. Lett.* **101**, 248002 (2008)
7. F.-L. Yang and Y.-T. Huang, New aspects for friction coefficients of finite granular avalanche down a flat narrow reservoir. *Granul. Matt.* **18**, 77 (2016)
8. C.-C. Lin, R. Artoni, F.-L. Yang, and P. Richard, Modelling the wall friction coefficient for a simple shear granular flow in view of the degradation mechanism. *J. Fluid Mech.* **969**, A7 (2023)
9. R. Artoni and P. Richard, Effective wall friction in wall-bounded 3D dense granular flows. *Phys. Rev. Lett.* **115**, 158001 (2015b)
10. F. Meng, M. Pang, S. Hua, H. Liu, L. Ma, Experimental study on nonlinear friction behavior of granular flow lubrication. *Phys. Rev. E* **105**, 105598 (2022)

Theses

11. T.-Y. Chiu, Direct and indirect measurements of the rheological property of steady dry granular flows down a rough incline, Master Thesis, National Taiwan University, Taiwan (2015)